Flame Interactions in Turbulent Premixed Twin V-flames.

T.D. Dunstan[1], N. Swaminathan*[1], K.N.C. Bray[1], N.G. Kingsbury[1]

[1] Department of Engineering, Cambridge University, Cambridge, CB2 1PZ, UK.

*Corresponding author:

Department of Engineering, Cambridge University,

Trumpington Street, Cambridge, CB2 1PZ, UK.

E-mail: ns341@cam.ac.uk.

Fax: +44(0)1223 765311.

Published in Combustion Science and Technology, 185, 134-159, 2013

(Authors' Preprint)

Running Title: Flame Interactions.

Abstract

Multiple flame-flame interactions in premixed combustion are investigated using Direct Numerical Simulations of twin turbulent V-flames for a range of turbulence intensities and length scales. Interactions are identified using a novel Automatic Feature Extraction (AFE) technique, based on data registration using the Dual-Tree Complex Wavelet Transform. Information on the time, position and type of interactions, and their influence on the flame area is extracted using AFE. Characteristic length and time scales for the interactions are identified. The effect of interactions on the flame brush is quantified through a global stretch rate, defined as the sum of flamelet stretch and interaction stretch contributions. The effects of each interaction type are discussed. It is found that the magnitude of the fluctuations in flamelet and interaction stretch are comparable, and a qualitative sensitivity to turbulence length scale is found for one interaction type. Implications for modelling are discussed.

Keywords: Flame Stretch, Wavelets, Dual-Tree Complex Wavelet Transform, Data Registration

1 Introduction

Lean premixed combustion offers much potential as a method of reducing emissions and increasing efficiency in combustion systems, but accurate modelling of turbulent combustion in this mode remains challenging. The sensitivity of these flames to small fluctuations in temperature or composition, and their susceptibility to thermo-acoustic instabilities present difficulties to the modelling and design of lean combustion systems. The role of flame interactions in turbulent premixed flames, although recognised as important (Borghi, 1990; Burluka et al., 1997; Kerstein, 2002), is not well understood at present.

The loss of flame due to flame interaction is an important design consideration for lean combustion systems. A number of studies have identified flame-flame interactions as one of the leading causes of combustion induced noise in laminar (Schuller et al., 2002; Candel et al., 2004; Talei et al., 2012) and turbulent (Balachandran et al., 2005) flames. The flame's sensitivity to the local thermo-chemical state can also lead to thermo-acoustic instabilities due to coupling between the pressure perturbations and rate of heat release (Balachandran et al., 2005).

In addition, novel low-emission modes of combustion such as MILD (Moderate or Intense Low-Oxygen Dilution), in which partially premixed reactants and pockets of exhaust gases are injected into the combustion chamber above the ignition temperature, show indications of flamelet type structures which undergo large numbers of flame interactions (Minamoto et al., 2011). In all of these situations, flame interaction phenomena need to be better understood to help model development.

Flame-flame interactions can be broadly categorised as either normal or counter-normal, where the flame normal is defined as positive in the direction of the fresh gases. Normal interactions occur when flames approach one another in the direction of propagation of the flame surface, and counter-normal interactions occur where turbulent straining acts to bring flame surfaces together against their propagation direction. In previous studies (Sohrab et al., 1984) these are commonly referred to as upstream and downstream interactions respectively, however, this terminology is avoided here to prevent possible confusion with the mean flow field.

For most configurations, normal interactions are more prevalent than counter-normal interactions due to the kinematics of the flame, but the outcome of both is similar - a rapid change in flame surface area and therefore the local rate of heat release. Normal flame interactions in simple one-dimensional geometries have been studied numerically using detailed chemistry (Echekki et al., 1996; Sun and Law, 1998). Chen et al. (1999) provide a detailed description of a single turbulence-generated normal flame interaction and pocket burn-out (where a pocket of fresh gas is consumed) using two-dimensional DNS with complex methane-air chemistry. Given a suitably defined isosurface within the reaction zone, three phases of the normal interaction process were identified: firstly, merging of the thermo-diffusive layers leading to the formation of a critical point where the isosurfaces meet and scalar gradients momentarily go to zero, resulting in the formation of two cusps and a pocket of fresh gas. Following this critical point, the highly curved cusps then retract into the fresh gases and the flame elements return to a flamelet type structure. The last phase, pocket burn-out, follows a similar pattern to that of the initial merger but with gradually increasing curvature adding to the final acceleration. According to the study of Chen et al. (1999), the shortest time scales for the initial interaction process - corresponding to the final stages of merger and the initial cusp recovery - are of the order of 1% of the characteristic laminar flame time, and so present a considerable challenge to numerical and experimental investigations.

Counter-normal interactions have been investigated experimentally and numerically for stationary flames in an opposed jet configuration (Sohrab et al., 1984; Lee and Chung, 1994; Kostiuk et al., 1999), and single events have been observed in unsteady DNS calculations (Hawkes and Chen, 2004). In general, unsteady counter-normal interactions result from incomplete combustion of the partially burnt gases in the region between two flame elements brought together by the surrounding turbulent strain field. This gradual extinction means that counter-normal interactions occur over longer time scales than normal interactions since they lack the flame acceleration and enhanced burning associated with the latter.

Central to the problem of studying multiple flame interactions is the ability to reliably extract information on individual interaction events from an unsteady flame simulation or experiment. In this paper a methodology is identified, described and applied to data produced using three-dimensional direct numerical simulation (DNS). The specific objectives of this study are:

1. To conduct DNS in a novel twin V-flame configuration, which provides a degree of control over the frequency of interactions in the central region of the flame brush.

2. To apply a novel post-processing technique based on the Dual-Tree Complex Wavelet Transform (DT-CWT).

3. To gather improved understanding on the type of flame interactions, their statistics and their contributions to either loss or gain of flame surface area.

The modelling of these effects is not attempted here and will be addressed in future.

The single V-flame configuration has been extensively studied, both experimentally (Shepherd, 1996; Anselmo-Filho et al., 2009) and numerically (Bell et al., 2005; Domingo et al., 2005), and so provides a well understood base configuration that can be readily extended to study interacting flames, and against which the interacting flame data may be compared.

In contrast to previous DNS studies on flame interactions, the focus here is on understanding the combined effect of multiple, transient interactions in three-dimensions, and on quantifying their role in the production or destruction of flame surface area. It should be noted that although the flame configuration clearly plays an important role in determining the probability of different types of interaction occurring, we presume that the individual interaction structure and progress is independent of the flame geometry, and therefore applicable to all flow configurations.

This paper is organised as follows: In Section 2, details of the simulation parameters and numerical methods are introduced. In Section 3, the Automatic Feature Extraction (AFE) technique, used to identify and extract information on individual flame interactions is described. Results are presented in Section 4, beginning with the physical and temporal distribution of the interactions in relation to the mean flame brush. In Section 4.5, the relations between flame interactions and changes in flame surface area are discussed. The conclusions are summarised in Section 5.

2 DNS Database

A schematic diagram of the twin V-flame configuration is shown in Fig. 1. All flames in this study were simulated using the DNS code SENGA2, an enhanced version of

SENGA1 (Jenkins and Cant, 1999). SENGA2 solves fully compressible conservation equations for mass, momentum, energy and $N - 1$ chemical species on a uniform Cartesian grid, where N is the total number of chemical species. A 10^{th} order central difference scheme is used for interior spatial derivatives and a 4^{th} order Runge-Kutta scheme advances the solution in time. Full details of the governing equations and numerical implementation can be found in Dunstan et al. (2011).

Chemistry is approximated by a single-step irreversible global reaction between reactants and products ($N = 2$), and the thermo-chemical state of the system is fully described by the progress variable, c, which varies monotonically from 0 in the fresh gases to 1 in fully burnt products. The reaction rate has an Arrhenius form with non-dimensional activation temperature $\beta = 7.13$. Although much of the chemical complexity of premixed flames is omitted by using a single-step reaction, it is an appropriate level of description for the phenomena of interest here. Results obtained with this approximation represent a generalisation of many possible compositions and, within the scope of this study, the results will therefore be applicable to other flames that conform to the thermo-chemical parameters used in this study. These parameters are summarised in table 1, and are representative of a lean, preheated hydrocarbon-air flame with unity Lewis number. The laminar flame thermal and diffusive thicknesses are respectively $\delta_{th} = 1/max|\nabla c|$, and $\delta = D/s_L$, where D is the temperature-dependent diffusivity of c and s_L is the unstretched laminar flame speed. $\tau_f = \delta_{th}/s_L$ is the laminar flame time scale, T_{in} is the temperature of the fresh gases at the inlet, and $\tau = (T_{ad} - T_{in})/T_{in}$ is the heat release parameter where T_{ad} is the adiabatic flame temperature. Although the value of $\tau = 2.52$ used in this study may appear low, it is typical for gas turbine combustion (Jones, 2011). In the rest of the paper all quantities are normalised appropriately using these flame parameters, and this is indicated by the superscript $^+$.

At the flame holders, shown in Fig. 1, the mass fractions are set to equilibrium product values ($c = 1$) and the velocity components are restricted to their mean inlet values through a Gaussian weighting function with an approximate radius of $R_{fh} \approx 1.16\delta_{th}$, as discussed in Dunstan et al. (2011). The flame holders are positioned at $x^+ \approx 3.5$ in all cases. The flame holder centre-to-centre separation is $d^+_{fh} \approx 5.8$. Following preliminary studies in two-dimensions, it was found that within the central region of the domain the two flame branches remain minimally correlated as long as $d_{fh} > l_0$, where l_0 is the integral length scale of the turbulence in the region close to the flame holders.

The influence of the flame holders on the statistical properties of the flames diminishes rapidly with downstream position. Previous investigations of single V-flames in three-dimensions (Dunstan et al., 2011) have shown that biases in the distributions of surface-conditioned tangential strain rate and curvature become negligible after a mean-flow convective time of $0.4\tau_f$. In the current simulations this corresponds to streamwise positions $x^+ > 10.1$. The relative influence of the flame holders will also diminish with increasing turbulence intensity, and so it is unlikely that any significant influence remains within the regions of interest for the flames presented here.

It should also be noted that no energy is added to the flow in the current implementation, and super-adiabatic flame temperatures cannot occur since equi-diffusive transport is assumed. Furthermore, no boundary layer is formed around the flame holder, and hence, no significant shear-generated turbulence which would otherwise produce strongly non-isotropic and inhomogeneous turbulence conditions downstream. While it is recognised that including these effects would more accurately reflect real V-flame behaviour, the intention here is not to recreate specific experimental conditions but to investigate the interaction process in a more general sense.

The boundary conditions on all non-periodic faces are based on Navier-Stokes Characteristic Boundary Conditions (NSCBC) (Poinsot and Lele, 1992). On the downstream and transverse faces the standard outflow NSCBC implementation has been modified to accommodate the strong transverse gradients and source terms generated by the flame (Sutherland and Kennedy, 2003; Yoo and Im, 2007; Dunstan et al., 2011), which ensures that stability and accuracy are preserved while allowing unsteady flame elements to cross the boundary. At the inlet, velocity components are interpolated from precomputed fields of fully-developed homogeneous isotropic turbulence at the desired turbulence intensity.

The domains have sides $L_x^+ = 29.7$ in the streamwise direction, $L_y^+ = 14.9$ in the transverse direction, and $L_z^+ = 26.0$ in the periodic direction. The grid resolution for cases TV06 and TV10 is $N_x = 672$, $N_y = 336$ and $N_z = 588$, and for case TVFS is $N_x = 684$, $N_y = 342$ and $N_z = 589$, giving a maximum (diagonal) grid point separation which is less than $\delta_{th}/13$. The time step was fixed at 2×10^{-8} s.

Three cases are considered; two with fixed integral length scale and different turbulence intensity, and one with fine scale turbulence, as summarised in Table 2, where u'_{in} is the inlet rms velocity fluctuation, and l_0 is the integral length scale in the frozen turbulence. The Karlovitz number is estimated from $Ka \approx (u'_{in}/s_L)^{\frac{3}{2}}(l_0/\delta)^{-\frac{1}{2}}$. The turbulent Reynolds and Damköhler numbers are $Re_{l_0} = u'_{in}l_0/\nu$ and $Da = \tau_{l_0}/\tau_f$ respectively, where ν is the kinematic viscosity of the fresh gases and $\tau_{l_0} = l_0/u'_{in}$. The turbulence parameters chosen in this study are intended to explore the sensitivity of flame interactions to changes in both turbulence intensity and turbulent length scale.

The regimes of turbulent combustion typically encountered in IC engines and gas turbines are successfully mimicked in the current simulations, however, it should be noted that the turbulent Reynolds and Damköhler numbers found in real systems are typically larger than those achieved here.

All simulations are run for two complete flow-through times, $2\tau^+_{FT} \approx 3.6$, and only data from the second flow through time are used for analysis. To further ensure that all initial transients have decayed and a statistically stationary state has been reached, global properties such as the total product mass fraction and total turbulent kinetic energy within the domain are tracked to confirm that they no longer vary significantly with time. In order to accurately reconstruct the interaction history, snapshots of the progress variable field were dumped at intervals of $\Delta t^+ = 0.023$. As noted in the introduction, the shortest relevant time scales for normal flame interactions based on changes to the displacement speed of an isosurface are of the order $0.01\tau_f$, which relates to both the final stages of isosurface merger, and the initial stages of cusp recovery immediately following the merger (Chen et al., 1999). Changes to the heat release rate occur over slightly longer time scales however - of the order of $0.03\tau_f$. The present sampling time interval of $0.023\tau_f$ is therefore sufficient to capture all such events, and the sensitivity of the results to this sample interval is discussed in more detail in Section 3.1.

3 Data Analysis

Mean flow variables are obtained by time and ensemble averaging, using 32 evenly spaced snapshots in time and all points in the periodic direction. For any variable

$Q(x, y, z, t)$:

$$\overline{Q}(x, y) = \frac{1}{S N_z} \sum_{m=1}^{S} \sum_{k=1}^{N_z} Q(x, y, k, t_m) \tag{1}$$

where S and N_z are the total number of snapshots in time, and nodes in the periodic direction respectively. In reacting flow simulations it is often more convenient to consider the density-weighted or Favre average of Q defined by $\widetilde{Q} = \overline{\rho Q}/\overline{\rho}$.

For even the simplest fuels, the interaction between two premixed flame elements is a multi-stage process involving widely differing time scales, as described in detail by Chen et al. (1999). In attempting to quantify the cumulative effect of a large number of these interactions, a degree of simplification is necessary and this is achieved here by reducing each interaction process to a discrete event. This simplification makes it possible to allocate a precise time and position to each interaction, and the frequency and distribution of these interactions can then be investigated.

To this end, we consider the topology of a single isosurface of the reaction progress variable at $c = 0.8$, which is close to the point of maximum heat release in the reaction layer, and is therefore most closely associated with changes in the rate of heat release and the preservation of a flamelet type structure. During run-time of the simulations the progress variable field is binarised around this value and saved for subsequent analysis using Automatic Feature Extraction (AFE) which is described next.

3.1 Automatic Feature Extraction

When considering only a single isosurface of c, the extraction of flame interactions is equivalent to identifying topological changes in the isosurface between snapshots at time t_i and t_{i+1}, where $t_{i+1} = t_i + \Delta t$. One way this can be done is by calculating certain topological invariants at successive time steps. For a simple surface embedded in a three dimensional field, these invariants, known as the Betti numbers, β_n, (Carlsson, 2009) have an intuitive interpretation: β_0 is the number of connected components, β_1 is the number of tubes or tunnels, and β_3 is the number of isolated pockets. The number and type of interactions taking place within the interval can then be described entirely by the changes to these numbers, provided care is taken to exclude boundary effects. However, such an analysis does not provide any information on the location of individual interactions within the domain, or on the magnitude of the interactions, where the magnitude in this context refers to some measure of the change in surface area, or volume enclosed by the isosurface.

To provide this additional information an alternative technique known as data registration is used. The specific method used in this study, developed by Chen and Kingsbury (2012), does not operate on the raw data directly, but first transforms the data into the wavelet domain using the Dual-Tree Complex Wavelet Transform (DT-CWT) (Kingsbury, 2001). The data registration procedure, and the relevant features of the DT-CWT are outlined in the remainder of this section. Details can be found in Chen and Kingsbury (2012) and Kingsbury (2001).

The topic of wavelet methods in fluid mechanics is a large and expanding field, and a complete description is beyond the scope of this paper. A good introduction can be found in Schneider and Vasilyev (2010), and for combustion problems in particular in Prosser and Cant (2011).

In general, wavelet decomposition involves a repeated convolution operation between an input function and an analysing wave form, and in this respect shares many similarities with the more widely used Fourier transform. In contrast to Fourier methods, however, the wavelet transform uses spatially compact wavelet functions which enables some of the spatial information to be retained along with the decomposition in wavenumber space.

The DT-CWT improves on the standard wavelet transform by employing complex valued wavelet coefficients to overcome certain well known deficiencies in the standard methods (Selesnick et al., 2005). For current purposes, the DT-CWT transform can be regarded as a computationally efficient multi-scale spatially resolved description of the original data, which uses 28 directionally selective filters per scale to determine the orientation of features to within approximately 2 degrees (Romberg et al., 2003) and enables features to be tracked between related data sets using the phase relations between the coefficients.

Once the data have been transformed into the complex wavelet domain, the data registration process proceeds through the construction of a transformation matrix that describes the translations and deformations that have occurred between the two data sets at t_i and t_{i+1} whilst allowing for topological differences (Chen and Kingsbury, 2012). This is an iterative process that begins at the largest (coarsest) scale of the transform and moves through successively finer scales until satisfactory alignment of the datasets has been achieved. In the present context this means that the effect of the first iteration is mainly to compensate for convection of the flame by the mean flow. Due to the relatively high streamwise mean velocity this first iteration will effectively be a solid-body translation of the entire data set at the mean inlet velocity $\overline{u}_{in}$. Having applied this first correction, subsequent iterations will then act on the smaller scale differences due to turbulent straining, curvature, and propagation of the flame surface.

Key to the successful application of this technique in the present context is its ability to identify interacting regions and exclude them from the construction of the transformation matrix. This is achieved by applying a weighting system to the transformation parameters based on the correlation between pairs of wavelet coefficients at each time step. In this way a low weighting will be given to pairs of coefficients where a feature (such as a flame surface element) exists only in one of the data sets, as would occur due to annihilation of flame elements following interaction. The specifics of this procedure for the current application are discussed in the remainder of this section. A flow-chart summary is given in Fig. 2, and an example of the procedure applied to two-dimensional test data is shown in Fig. 3.

The AFE procedure used here comprises three principal stages: (1) the binarised c field data from two successive time steps at t_i and t_{i+1} (Fig. 3a), denoted Ψ_i and Ψ_{i+1} respectively, are transformed into the wavelet domain; (2) the wavelet coefficients at successively finer levels of resolution are then used to construct the transformation matrix, described above, which is then applied to the source data set, Ψ_i, to align it with the target data set, Ψ_{i+1}, to produce the registered data set Ψ_i' (Fig. 3b); (3) a series of logical operations is then applied to the data set pair Ψ_i' and Ψ_{i+1}: first, the set-theoretical difference, $\Phi = \Psi_{i+1} - \Psi_i'$, is obtained, which represents the change in burnt gas volume that has occurred over the interval (Fig. 3c). The change in flame area associated with Φ is then found by extracting the subset, ϕ, representing the edge points of Φ. The set ϕ is then conditioned on the data sets, Ψ_{i+1} and Ψ_i' respectively, to determine whether the points in ϕ originate from the data at t_i or t_{i+1}. The difference between the resulting conditioned data sets, $\phi_i = \phi \cap \Psi_i'$ and $\phi_{i+1} = \phi \cap \Psi_{i+1}$ therefore represents the change in flame area that has occurred between times t_i and t_{i+1}. In practice, the alignment of the datasets is not perfect and so when conditioning is carried out it is necessary to include a tolerance of 2-3 grid points in any direction. Due to the high resolution of the flame, however, this has a negligible effect on the flame area estimate.

Since the contributions to the area change from convection or turbulent straining are removed by the alignment and differencing operations described above, the sets ϕ_i and ϕ_{i+1} represent the changes in area purely due to the topological changes caused by flame interactions.

Information on the time, position and type of interactions can also be derived from the AFE data:

- The precise time of occurrence of each interaction within an interval Δt cannot be known exactly. However, it can reasonably be assumed that, overall, the interactions will be evenly distributed throughout the intervals, and so the midpoint $t = t_i + \Delta t/2$ is taken as the time of interaction in all cases studied here.

- The spatial location of the interactions can be approximated by taking the average position of all points in the set ϕ associated with an individual interaction; which is equivalent to calculating the centroids of the extracted burnt gas regions in Φ. Assuming that the flame surface retracts approximately symmetrically about the interaction point, this provides a good estimate for the actual positions of the interactions.

- While the exact type of interaction could in principal be determined automatically from ϕ, for example by calculating the topology of the flame elements before and after merger, or by tracking the changes in flame normals, in practice it was found that simple inspection of the extracted data provided a straightforward and unambiguous method for the flames studied here. Details of the interaction types and their identification are given in Section 4.1.

There are some inherent uncertainties in the above method that should be kept in mind, and these come from two main sources: the first is due to inaccuracies in the data registration scheme, and to the approximations and tolerances introduced in estimating the change in flame area, ΔA, from the data sets Ψ_i' and Ψ_{i+1}. The second arises from sensitivity to the sample interval Δt. The first source is relatively minor since the registration scheme is iterative and thus it can achieve any desired level of accuracy.

The more fundamental source of uncertainty is the sensitivity of the extracted data sets to changes in the sample interval Δt. Clearly, when trying to characterise a transient process using discrete samples of the data there is no well-defined ’correct’ value for this interval. However, much of this sensitivity can be avoided by considering the global stretch rate, $K = (dA/dt)/A$, where A is the total flame area within the sample region at a given time, rather than the absolute area change, since the time increment is then automatically taken into account in the denominator. Details of its use in the current context are given in Section 4.5.

In spite of this, some sensitivity to Δt is still expected in K, since the area changes associated with interactions are non-linear. An appropriate value of Δt must therefore be chosen, and since the aim of this study is to examine the non-flamelet contribution of flame interactions, this remaining sensitivity can be minimised by considering the time scale analysis conducted by Chen et al. (1999). In this study it was found that the time scale over which 95% of the increase in the heat release rate occurs during interaction is of the order $0.03\tau_f$. Using this as an indicator for the time scale over which non-flamelet like behaviour occurs, a reasonable choice for Δt for the purposes of extracting non-flamelet contributions would therefore be $\Delta t < 0.03\tau_f$. Larger values than this will include changes in flame area that are caused by normal turbulent processes such as straining and curvature. Smaller values would be acceptable but rapidly become computationally prohibitive, and would require that results are summed over a number of intervals to estimate the total contribution. The present values of $0.02\tau_f$ therefore represents a compromise between these two limits.

4 Results

A snapshot of the $c = 0.8$ isosurfaces overlaid with contours of $\tilde{c}$ is shown in Fig. 4a for the flame TV06, which illustrates the typical scales of wrinkling and the relation between the instantaneous and mean progress variable fields. Based on the inflow turbulence characteristics, all the flames in the current database fall within the Thin Reaction-Zones (TRZ) regime according to the modified regime diagram of Peters (2000). In this regime, Kolmogorov scale eddies are able to penetrate and distort the preheat zone of the flame causing significant wrinkling of the flame front, but are unable to significantly disrupt the inner reaction layer. As noted above, these estimates are based on the turbulence properties at the inlet, and so represent the upper limit of the expected regime. Fig. 4b shows the decay of u'/s_L along the centre-lines ($y^+ = 7.44$) for all the flames, and it can be seen that the actual turbulence experienced by the flames is considerably lower than the nominal inlet values, particularly for the rapidly dissipating fine-scale turbulence in TVFS. However, visual inspection of the progress variable fields has shown that the TRZ regime is a good description of the flame. Even in the highest intensity case where the flame is strongly stretched by the flow, breaches in the reaction layer are caused only by interactions and not turbulent stretching. Exceptions to this are counter-normal type interactions to be discussed below.

4.1 Interaction Types

From the current database four distinct interaction types can be identified according to the local topological changes. These are shown schematically in Fig. 5. As noted in the introduction, a first distinction can be made between normal and counter-normal interaction types: The flame normal, $\vec{N}$, defined as positive towards the fresh gas, $\vec{N} = -\nabla c / |\nabla c|$, indicates the direction in which an unstrained planar laminar flame will propagate relative to the surrounding fluid. Normal interaction therefore refers to cases where flame elements approach one another in the direction of propagation, whereas counter-normal interaction describes cases where flame elements are brought together against their direction of propagation by the surrounding strain field. Normal type interactions can be further divided into three sub-types: convex-normal (CX), tunnel closure (TC), and pocket burn-out (PB). In Fig. 6, examples of the extracted data sets ϕ_i and ϕ_{i+1} obtained using AFE for each interaction type are shown.

For the current database this categorisation is complete in the sense that all interactions that occur can be unambiguously assigned to one of these categories. It should be noted that while it is theoretically possible that TC and PB type events also occur in the counter-normal direction no such events were observed in the simulations presented here.

The reason for using this method of classification comes from considering the differences in the local stretch rate experienced by the flame elements before and after merger occurs. The local stretch rate of an isosurface, κ, can be written as $\kappa = a_T + s_d C$, where a_T is the tangential strain rate, s_d is the propagation speed of the isosurface in the flame normal direction, and $C = \nabla \cdot \vec{N}$ is the total curvature, defined as positive when the flame is convex towards the fresh gas. The stretch rate is a leading order parameter in determining the displacement speed s_d of a flame element. For small stretch rates the displacement speed s_d varies approximately linearly with κ (Williams, 1994), whereas for high stretch rates, such as those induced by strong curvature, the response of the displacement speed can be highly non-linear, particularly for fuels with non-unity Lewis numbers. For the purpose of understanding the effects of interactions, it is therefore important that the method of classification reflects the underlying differences in the strain and curvature experienced by the isosurfaces.

It can be seen from Figs. 5 and 6 that each interaction type can be associated with distinct curvature characteristics of the flame elements prior to merger. These curvature characteristics can be described most succinctly by considering the two principal curvatures of each flame element (Pope et al., 1989), where +ve (-ve) values indicates convex (concave) curvature towards the fresh gases. For each of the interaction types, the following points can be made:

- **CN** (counter-normal): Quasi-1D interaction. Principal curvatures -ve, -ve. Weak or weakly negative principal curvatures due to the kinematic restoration of the flame. Effects of tangential straining are dominant.

- **CX** (convex-normal): Quasi-1D interaction. Principal curvatures +ve, +ve. Both curvature and tangential straining can be significant.

- **TC** (tunnel-closure): Quasi-2D interaction. Principal curvatures -ve, +ve (or ≈ 0). Increasing negative first principal curvature dominates the stretch rate prior to merger.

- **PB** (pocket burn-out): Fully 3D interaction. Principal curvatures -ve, -ve. Increasing negative curvatures in both principal components dominates the stretch rate prior to merger.

In all types except PB interactions, large curvature magnitudes follow cusp formation (either positive curvatures for CN interactions or negative curvatures for CX and TC interactions) and so will also determine the flame behaviour after isosurface merger has occurred. Curvature is therefore the key factor determining the rate of change of flame area at all stages of the interaction process. The method of classification proposed here therefore provides a simple and unambiguous method of capturing these differences without the need to directly evaluate local curvatures.

4.2 Position of Interactions

Figure 7 shows the positions of all interactions occurring within the simulation period collapsed on to the $x - y$ plane, together with contours of the Favre-averaged progress variable, $\tilde{c}$, for all cases. The differences in turbulence intensity and length scale between the cases are reflected in the $\tilde{c}$ fields. Studies of single turbulent V-flames under comparable conditions to flames TV06 and TV10 have shown that the growth of the flame brush downstream of the flame holder is well described by simple Taylor type turbulent diffusion (Dunstan et al., 2011). The flame TVFS, however, does not follow this trend: the local turbulent time scales along the centre line are similar to the flame TV10 (see Section 4.3 below) and so the flame should display a similar rate of growth of the flame brush thickness if the Taylor hypothesis holds. In this case, it appears that since the turbulence length scale for the flame TVFS is small ($< \delta_{th}$), the energy containing eddies are unable to strain and curve the flame front as effectively as in the flames TV06 and TV10, and in addition will be more rapidly dissipated due to viscous effects. This results in a more weakly perturbed, and therefore slower, turbulent flame than the turbulence parameters might suggest.

It can be seen that for all flames the majority of normal interactions occur in the central region of the domain where the two flame branches interact, as anticipated. In contrast, all CN events are located in the wakes of individual flame holders. Counter-normal interactions can only occur when strong compressive normal strain rates persist over a sufficiently large space and time to include two individual flame fronts, and have sufficient magnitude to overcome the effects of normal flame propagation and dilitation due to heat release. It is probable that these conditions are created by pairs of counter-rotating vortices on either side of the flame, and are therefore somewhat dependent on the geometry of the flame holder; in this case on the flame holder diameter which determines the proximity of the flame fronts immediately downstream, and hence the likelihood of CN interactions.

Two features of the distributions of the normal interactions in Fig. 7 are worth noting. First is that despite the differences between the distributions of the interactions in physical space for each of the flames, the distributions in $\tilde{c}$ space are very similar, with the most likely position for CX type interactions occurring close to the middle of the flame brush for all the flames. This is illustrated in Fig. 8 which shows the number of interactions of each type that occur within equally-spaced bins of $\tilde{c}$. The reason for this clustering of CX interactions around $\tilde{c} = 0.5$ can be understood by considering the definition of the Flame Surface Density (FSD), $\Sigma_{c^*=0.8}$, which represents the expected amount of flame area per unit volume at a given location: $\Sigma_{c^*=0.8} = (\overline{|\nabla c|}_{c^*=0.8})P(c^*)$, where $P(c^*)$ is the probability of finding $c^* = 0.8$ at a given spatial location (Pope, 1988). The mean conditional gradient, $\overline{|\nabla c|}_{c^*=0.8}$, does not change significantly through the flame brush, and so $\Sigma_{c^*=0.8}$ is determined principally by the probability $P(c^*)$. For all the flames presented here the value of $\Sigma_{c^*=0.8}$ and therefore $P(c^*)$ peaks around $\tilde{c} = 0.5$ (not shown), in agreement with many previous results for flames in the thin-reaction-zones and corrugated-flamelets regimes (Driscoll, 2008). The probability of flame interaction can be viewed as the joint probability of two statistically-independent flame elements occupying the same region at the same time, and so it may be expected that interaction activity follows $\Sigma_{c^*=0.8}$ provided the flame branches are statistically uncorrelated. For the present flames, the statistical independence of the flame branches is maximised by ensuring $l_0/d_{fh} < 1$, where d_{fh} is the flame holder separation shown in Fig. 1. It is important to note, however, that as the flames approach one another they begin to experience the same flow field regardless of their initial separation, and so complete statistical independence cannot occur in practice.

The second important feature of the distributions in Figs. 7 and 8 is the separation between the clusters of different interaction types, occurring in the sequence CX → TC → PB with downstream position. This suggests that interaction types occur in a cascade with the spatial separation resulting from a delay between interaction types combined with the mean convection velocity in the streamwise direction. This cascade behaviour arises because of the loose causal connections between the interaction types, and while a one-to-one mapping between events is not possible, some general points can be made bearing in mind the current flame geometry: the creation of a tunnel of fresh gas must be preceded by a CX type interaction in this configuration (assuming the isosurfaces are always connected at some point further downstream), and therefore TC events cannot occur unless preceded by at least one CX event. Once a tunnel is created at least one TC event must occur (unless there is local extinction), although multiple TC events are possible. In addition, isolated fresh gas pockets, although theoretically can be formed from a single CX event, are almost always formed following simultaneous TC events along a single tunnel in the simulations investigated here. This provides a second causal link between TC and PB type events.

4.3 Delay Time

It is possible to identify approximate characteristic delay times between the interaction types by constructing correlation coefficients between the interaction histories subject to a time offset of Δ^+. To do this, we first define the function $\chi_i(t^+)$ as the number of interactions occurring over a fixed interval[1] for each interaction type, where i = CX, TC or PB. The statistical correlation can then be calculated between pairs of χ_is of different type after introducing a time shift of Δ^+ to one of the functions: $corr(\chi_i(t^+ + \Delta^+), \chi_j(t^+))$. If the two functions are unrelated the correlation will be close to zero for all Δ^+, however, for related functions a peak in the correlation indicates the Δ^+ value corresponding to the characteristic delay time between the two interaction types. Choosing $i = j$ produces the auto-correlation of $\chi(t^+)$ which will have a peak value of 1 at $\Delta^+ = 0$ and decrease to zero with increasing Δ^+, however, our present interest is in $i \neq j$. The results are shown in Fig. 9 for the correlations between CX and TC events, where the standard Pearson product-moment method has been used to evaluate the correlation coefficients. Correlations involving PB interactions are not included since many of the flame pockets are convected out of the domain before interactions can occur.

It can be seen in Fig. 9 that in general the delay times for each flame are dependent on the turbulence intensity and length scale, with characteristic times of approximately

---

[1] The interval used to evaluate χ_i is approximately 2 to 3 times the AFE interval Δt. This is done to compensate for the relatively small number of interactions occurring within each Δt, and within this range the results are insensitive to the exact value used.

0.1, 0.06, and 0.04 for flames TV06, TV10, and TVFS respectively. Considering the turbulence intensity near the $\tilde{c}$ isoline where the majority of CX interactions occur, the normalised large eddy turn over times (the local Damköhler numbers) in this region, $\tau^+_{l_0} = (l_0 s_L)/(u' \delta_{th})$, are approximately 1.24, 0.55, and 0.53 for TV06, TV10, and TVFS respectively. Thus, there is an almost linear relationship between $\tau^+_{l_0}$ and the characteristic delay times for these flames. This result suggests that it is turbulent convection of the flame elements, and not the scales of wrinkling that determines the delay time, since there is no observable effect on the delay time from differences in the turbulent length scales alone. It should also be noted that thermo-diffusive properties of the flame are also likely to be an important factor affecting the interaction delay time, however, since these properties are the same in all the flames studied here this cannot contribute to the observed variation.

4.4 Interaction Length Scales

It is possible to identify characteristic length scales for the interactions from the extracted volume, Φ, and surface, ϕ, data obtained using AFE. These are the volume based length scale, $L^{V+}_{int} = \Phi^{1/3}$, and the surface-area based length scale, $L^{S+}_{int} = \phi^{1/2}$, where the superscript + indicates normalisation by δ_{th}. In general these are not the same, and indeed a third possible length scale, the volume to surface-area ratio, $L^{R+}_{int} = (L^{V+}_{int})^3/(L^{S+}_{int})^2$, also provides information on the sphericity of an object since it is a function of both the size and shape of the extracted region, and which for a given volume reaches its maximal value only for a perfect sphere.

Table 3 gives the mean values of L^{V+}_{int} and L^{S+}_{int} for all flames by interaction type. Typical probability density functions for L^{V+}_{int} and L^{S+}_{int} for CX and TC type interactions are shown in Fig. 10. Comparing first the different flame cases, it can be seen that the only significant change in mean length scales occurs for CX type interactions, as in Fig. 10a for the TVFS flame, which is smaller than in the other two cases by approximately 15% - 20% due to the finer scale wrinkling in the TVFS flame. No such difference exists for the other interaction types, for example see Fig. 10b for TC type interactions, suggesting that length scales for TC and PB interactions do not strongly depend on either the turbulence intensity or the integral length scale. CN type interactions produce the smallest length scales, as one might expect, whereas the length scales of all normal type interactions are comparable, as one can see in Table 3. The ratio of L_{int}^{V+} to L_{int}^{S+} is similar for CN, CX and TC interactions for all the flames. This ratio, however, for PB type interactions is considerably different compared to other interaction types (about 0.42 for PB compared to 0.35 for other types). The value of about 0.42 (*cf.* 0.455 for a perfect sphere) reflects the tendency for pockets of thermo-diffusively stable flames to approach a spherical shape prior to burn-out.

4.5 Flame Area Change

A key question from the point of view of incorporating flame interactions into a combustion model is their effect on the rate of heat release in the flame. Under the flamelet assumption this is equivalent to assessing the change in flame area since, to leading order, this determines the overall rate of combustion. As outlined in Section 3.1, it is more appropriate to consider the rate of change of area as quantified by the stretch rate, rather than the absolute change in flame area. For the present analysis a global stretch rate, K, is used, which, in contrast to the locally defined stretch rate, κ, includes all area changes that occur within the sample regions indicated in Fig. 7. In this way, flame interactions, which are not precisely localised events, can be included in the analysis. The global stretch rate, $K = (dA/dt)/A$, can then be written as a sum of flamelet, K_F, and interaction, K_{INT}, contributions. Over the discrete time interval, Δt, these are given by:

$$K = \frac{2(A_{i+1} - A_i)}{(A_{i+1} + A_i)\Delta t} \tag{2}$$

and

$$K_{INT} = \frac{2(\phi_{i+1} - \phi_i)}{(A_{i+1} + A_i)\Delta t} \tag{3}$$

where $K_F = K - K_{INT}$, A_i and A_{i+1} are the total isosurface areas within the sample region at t_i and t_{i+1} respectively, and $(\phi_{i+1} - \phi_i)$ is the total change in area due to all interactions occurring in the interval, obtained using the AFE process outlined in Section 3.1. In the above definitions, the average value of A over the interval is used in the denominator, however, the results do not change significantly if A_i or A_{i+1} are used instead. The interaction stretch may also be decomposed by type, where: $K_{INT} = K_{CN} + K_{CX} + K_{TC} + K_{PB}$.

Figures 11a-c show the stretch rates defined above as a function of time for all cases. In general it can be seen that the largest contribution to the total stretch rates comes from the flamelet component, K_F, in all cases, and can take positive or negative values. In contrast, the total interaction contribution, K_{INT}, is smaller in magnitude and almost always negative except for flame TVFS where small positive contributions also occur.

Considering the interaction contributions by type, it can be seen that the largest negative stretch rates, and hence the largest contributor to flame area destruction, comes from TC type events for all the flame considered here. CN type events produce the smallest overall contribution, both because they are relatively rare in this configuration, and also individually smaller in magnitude.

CX type interactions can result in both positive or negative stretch rates. This is particularly notable in flame TVFS where the K_{CX} fluctuations are predominantly positive, in contrast to both the other cases. The reason for this dual effect of CX type interactions can be understood by considering changes to the local stretch rate, κ, as defined in Section 4.1, and in particular, the acceleration of the flame elements prior to merger combined with their curvature properties. Since the displacement speed of the flame, s_d, increases rapidly as the flames merge, if the flame elements are positively curved during this phase the result is a rapid increase in the curvature-induced stretch. Acceleration of the flame elements also occurs in TC and PB interactions, however, in these cases the curvature is predominantly negative, which leads to negative local stretch rates and a loss of area. During CX interactions, flame area is lost only after the merger of the $c = 0.8$ isosurface, due to cusp retraction. This loss is generally greater than the initial gain for all the flames studied here except TVFS. It can also be seen from Fig. 11 that this difference between the cases appears only in the magnitude of the net-negative CX interactions, which suggests that only the cusp retraction phase is sensitive to the turbulence length scale.

PB type interactions, similar to TC type interactions, are universally negative due to the negative curvature of the flame elements prior to merger, as outlined above. Although similar in magnitude to TC interactions, PB interactions are less frequent principally due to the lower frequency of pocket formation compared to tunnels, but also due to some loss of pockets though the downstream boundary. For the TV06 and TV10 flames these lost pockets account for less than 25% of the total formed, however, for TVFS this rises to over 50% and so the data on these events should be treated with caution.

To quantify the overall effects of interactions on changes in flame area, two quantities are of interest: the time-average and root-mean-squared (rms) values of the global stretch rates. These are summarised in Table 4. For statistically stationary flames such as these, the average global stretch rate, $\overline{K}$, is expected to be zero, which implies that $\overline{K}_F$ and $\overline{K}_{INT}$ must balance one another. In spite of the wide differences in the magnitudes of their respective fluctuations, this is approximately true for all the flames considered in this study. The residuals seen in $\overline{K}$ reflects a lack of statistical convergence in the data, however, this does not significantly affect any of the observations made here. TC events produce the largest average negative stretch rates, followed by approximately equal contributions from CX and PB type interactions. The exception to this is $\overline{K}_{CX}$ for flame TVFS which is positive, as discussed above.

While time-averaged values provide information on the expected biases for the stretch rates, the instantaneous effects of interactions are also of interest, and to assess this it is useful to consider the rms values of K_F and K_{INT}. These are given in Table 4, where it can be seen that, although instantaneous fluctuations in K_F are the largest contributor, the fluctuations in interaction stretch are also significant, and reach approximately 28%, 26%, and 17% of the K_F^{rms} values for flames TV06, TV10, and TVFS respectively. The modelling of these effects will be addressed in future work, however, from a phenomenological perspective the main points can be summarised as follows:

- CN type interactions do not contribute significantly to changes of flame area in the current configuration, since they are both less frequent and smaller in magnitude than other types. These two factors are related: vortices having sufficient power to overcome the normal flame propagation and expansion of the burnt gases are relatively rare, and since the interaction occurs over longer time scales due to the lower approach velocity of the flame elements compared to normal interactions, a smaller area change will be recorded over any particular sample interval.

- CX type interactions can lead to a net negative or positive change in the flame area, both in instantaneous and averaged values. The current results suggest that the cause of this qualitative change is related to the turbulence length scale, l_0/δ_{th}, where smaller length scales are associated with increases in flame area for this type of interaction. The local Damköhler number does not appear to be important since these are very similar for flames TV10 and TVFS.

- TC type interactions are responsible for the majority of flame area loss in all cases. They are both more frequent and have a larger average magnitude than the other interaction types.

- PB type interactions are similar in average magnitude to negative CX interactions, and make a similar overall contribution to the loss of flame area. Taking into account the convection of some pockets through the downstream boundary, their actual effect on the flame brush may be slightly larger.

- The frequency of CX and TC interactions both vary proportionally with turbulence intensity in the interacting region for the TV06 and TV10 flames ($N_{CX} \approx 10u'/s_L$ and $N_{TC} \approx 12u'/s_L$, where N is the number of interactions per τ_f). However, interactions in the TVFS flame do not follow the same trend ($N_{CX} \approx 12u'/s_L$ and $N_{TC} \approx 8u'/s_L$), which marks a qualitative change compared to the flames with larger turbulence length scales. As noted in Section 4.2, the occurrence of CX interactions can be associated with the joint probability of finding two flame elements at the same location, and so does not depend on the structure of the turbulence directly but only on the statistical distributions of the flame front. In contrast, TC type interactions depend more directly on the time and length scales of the turbulence, as evidenced by the delay-time dependence on the Damköhler number described in Section 4.2.

5 Summary and Conclusions

Direct numerical simulations of twin turbulent V-flames were carried out to investigate the phenomenology of multiple flame interactions in premixed turbulent flames. Flame interactions were defined by the topological changes to a single isosurface of the progress variable near the point of maximum heat release. A novel post-processing technique involving data registration in the complex wavelet domain was applied in order to extract information on the time, position and change in flame area associated with individual interactions. Three flames at different values of turbulence intensity and length scale were analysed to assess the sensitivity of the interactions to turbulence parameters.

Four distinct types of interaction were identified, based on topological changes to the flame surface: one counter-normal (CN), and three normal: convex normal (CX), tunnel closure (TC), and pocket burn-out (PB). The peak of CX type activity was found to coincide with the position of maximum flame surface density in the flame brush for all flames, in accordance with the expected behaviour for uncorrelated flame branches. Normal interactions were observed to occur in the cascade CX $\rightarrow$ TC $\rightarrow$ PB, due to the causal links between the interaction types. Characteristic delay times between the CX and TC types were found to be proportional to the large eddy time scale (or Damköhler number) in each case, suggesting that the turbulent convection of flame elements plays an important role both before and after the initial CX interactions. Characteristic length scales for the interactions were identified using the extracted volume and surface area data. The only significant difference in mean length scale magnitude was found for CX type interactions in flame TVFS, which were between 15% and 20% lower than those for flames TV06 and TV10. Other interaction types showed no significant sensitivity to turbulence intensity or turbulence length scale for the conditions considered here.

The effects of interactions on the turbulent flame brush were investigated by considering the global stretch rate of the flame, expressed in terms of a flamelet component, K_F, which includes the effects of turbulent straining and curvature-propagation, and an interaction component, K_{INT}, representing the area changes associated with flame interactions. It was found that TC type interactions are responsible for the majority of the overall flame area loss due to interactions. CN interactions are relatively rare and occur over longer time scales compared to normal interactions, and so do not contribute significantly to the total flame area change in the simulations studied here. CX type interactions can lead to either a net increase or net decrease in the flame area. The data suggest that the overall sign of CX contributions depends on the turbulence length scale, where smaller length scales are associated with a net increase in area, but no Damköhler number dependence was observed for these flames. Time-averaged values of stretch show that $\overline{K}_F$ and $\overline{K}_{INT}$ approximately balance, yielding $\overline{K}$ close to zero, as expected for the stationary flames studied here. The rms values of the stretch rates also indicate that interactions play a significant role in the instantaneous flame brush dynamics, with values for K_{INT}^{rms} of 28%, 26%, and 17% of the rms values of the flamelet stretch component for flames TV06, TV10, and TVFS respectively. The total and individual mean contributions to negative flame stretch correlate well with the inlet turbulence Reynolds numbers for the flames considered in this study.

For the purposes of model development, the following observations can be made regarding the present results:

- In the thin-reaction-zones regime, the overall contribution to flame area reduction from the non-flamelet processes is comparable to the better understood flamelet mechanisms involving strain and curvature. Many FSD based flamelet models employ a single destruction term to account for both the flamelet and non-flamelet contributions. However, given the fundamentally different physical processes underlying the two mechanisms, and their comparable importance in the flames studied here, it is likely that treating these effects separately would provide a firmer basis for modelling.

- The majority of the loss of flame area due to interactions (from TC types) does not tend to occur at the same position within the flame brush at which the initial interactions (CX) take place. Furthermore, the different interactions do not share the same phenomenology; with CX type interactions appearing to depend only on the statistical distribution of flame elements, but TC events also showing sensitivity to the turbulence time scales through a Damköhler number dependence. This implies that in order to adequately predict and capture the effects of flame interactions, factors which account for the observed delay times between interaction types and their different causal dependencies may need to be incorporated into the model.

Finally, the limitations of the single-step unity Lewis number assumption used in this study should be noted. While all the phenomena presented here are essentially fluid-mechanical in origin and adequately described by a global reaction mechanism, some important additional effects cannot be addressed. For sub-unity Lewis number flames the preferential diffusion of light fuel species or radicals ahead of the flame in positively stretched flame elements is expected to occur. This reduced thermo-diffusive stability is likely to increase the occurrence of net-positive area changes associated with CX type events. For the same reason, the cusp retraction phase following all types of interaction, where the flame cusps exhibit extreme positive curvature, is likely to be attenuated compared to unity Lewis number flames. Conversely, for super-unity Lewis number flames the opposite trends are expected. The influence of non-unity Lewis numbers on the propagation speed may also alter the interaction time scales, however, it is unclear how differences in steady-state characteristics of these flames will translate to the highly transient phenomena of interest here. A full investigation of these effects will be addressed in a future publication.

Another important topic to be considered is the role of flame interactions in the production of pollutants such as CO and NO_X. In this regard, it is likely that CN type interactions will have much greater importance than their effect on flame area would suggest, due to the importance of the burnt-gas side of the flame front for CO oxidation (Hawkes and Chen, 2004).

The twin V-flame configuration together with the methodology for extracting information on flame interactions outlined in this paper, provide a good framework to study these phenomena. The degree of control available over the type and intensity of interactions, and the realisability of the configuration in both computational and experimental settings make it well suited to investigating the role of interactions.

Acknowledgments

The authors would like to thank Professor R. S. Cant for the use of SENGA2. EPSRC funding through grant number EP/F028741/1, and funding from Rolls-Royce is acknowledged.

References

P. Anselmo-Filho, S. Honchreb, R.S. Barlow, and R.S. Cant. Experimental measurements of geometric properties of turbulent stratified flames. *Proc. Combust. Inst.*, 32:1763–1770, 2009.

R. Balachandran, B. O. Ayoola, C. F. Kaminski, A. P. Dowling, and E. Mastorakos. Experimental investigation of the nonlinear response of turbulent premixed flames to imposed inlet velocity oscillations. *Combust. Flame*, 143:37–55, 2005.

J. B. Bell, M. S. Day, I. G. Shepherd, M. R. Johnson, R. K. Cheng, J. F. Grcar, V. E. Beckner, and M. J. Lijewski. Numerical simulation of a laboratory-scale turbulent V-flame. *P. Natl. Acad. Sci. USA*, 102:29:10006–10011, 2005.

R. Borghi. Turbulent premixed combustion: Further discussions on the scales of fluctuations. *Combust. Flame*, 80:304–312, 1990.

A. A. Burluka, A. Gorokhovski, and R. Borghi. Statistical model of turbulent premixed combustion with interacting flamelets. *Combust. Flame*, 109:173–187, 1997.

S. Candel, D. Durox, and T. Schuller. Flame interactions as a source of noise and combustion instabilities. *AIAA J.*, 2004-2928, 2004.

G. Carlsson. Topology and data. *Bull. Amer. Math. Soc.*, 46:255–308, 2009.

H. Chen and N. G. Kingsbury. Efficient registration of non-rigid 3-D bodies. *IEEE T. Image Process.*, 21:262 – 272, 2012.

J. H. Chen, T. Echekki, and W. Kollmann. The mechanism of two-dimensional pocket formation in lean premixed methane-air flames with implications to turbulent combustion. *Combust. Flame*, 116:15–48, 1999.

P. Domingo, L. Vervisch, S. Payet, and R. Hauguel. DNS of a premixed turbulent V flame and LES of a ducted flame using a FSD-PDF subgrid scale closure with FPI-tabulated chemistry. *Combust. Flame*, 143:566–586, 2005.

J. F. Driscoll. Turbulent premixed combustion: Flamelet structure and its effect on turbulent burning velocities. *Prog. Energ. Combust. Sci.*, 34:91–134, 2008.

T. D. Dunstan, N. Swaminathan, and K. N. C. Bray. Geometrical properties and turbulent flame speed measurements in stationary premixed V-flames using direct numerical simulations. *Flow Turbul. Combust.*, 87:237–259, 2011.

T. Echekki, J. H. Chen, and I. Gran. The mechanism of mutual annihilation of stoichiometric premixed methane-air flames. *Twenty-Sixth Symposium (International) on Combustion*, 26:855–863, 1996.

E. R. Hawkes and J. H. Chen. Direct numerical simulation of hydrogen-enriched lean premixed methaneair flames. *Combust. Flame*, 138:242–258, 2004.

K. W. Jenkins and R. S. Cant. DNS of turbulent flame kernels. In *Proceedings of the Second AFOSR Conference on DNS and LES*, pages 192–202, 1999.

B. Jones. Application of lean flames in stationary gas turbuines. In N. Swamianthan and K.N.C. Bray, editors, *Turbulent Premixed Combustion*. Cambridge University Press, 2011.

A. R. Kerstein. Turbulence in combustion processes: Modeling challenges. *Proc. Combust. Inst.*, 29:1763–1773, 2002.

N. G. Kingsbury. Complex wavelets for shift invariant analysis and filtering of signals. *J. Appl. Comput. Harmon. Anal.*, 10:3:234–253, 2001.

L. W. Kostiuk, I. G. Shepherd, and K. N. C. Bray. Experimental study of premixed turbulent combustion in opposed streams. part III: spatial structure of flames. *Combust. Flame*, 118:129–139, 1999.

S. D. Lee and S. H. Chung. Experimental investigation of the nonlinear response of turbulent premixed flames to imposed inlet velocity oscillations. *Combust. Flame*, 98:80–92, 1994.

Y. Minamoto, T. D. Dunstan, and N. Swaminathan. DNS of EGR-type combustion in MILD condition. *7th Mediterranean Combustion Symposium, Sardinia*, 1:TC39, 2011.

N. Peters. *Turbulent Combustion*. Cambridge University Press, 2000.

T. Poinsot and S. Lele. Boundary conditions for direct simulations of compressible viscous flows. *J. Comput. Phys.*, 101:104–129, 1992.

S. B. Pope. The evolution of surfaces in turbulence. *Int. J. Engng. Sci.*, 26:445–469, 1988.

S. B. Pope, P. K. Yeung, and S. S. Girimaji. The curvature of material surfaces in isotropic turbulence. *Phys. Fluids A*, 1(12):2010–2018, 1989.

R. Prosser and R. S. Cant. Wavelet methods in computational combustion. In T. Echekki and E. Mastorakos, editors, *Turbulent Combustion Modeling*. Springer, 2011.

J. Romberg, M. Wakin, H. Choi, and R.G. Baraniuk. A geometric hidden Markov tree wavelet model. In *Proc. Wavelet Applications Signal Image Processing X (SPIE 5207), San Diego*, pages 80–86, 2003.

K. Schneider and O.V. Vasilyev. Wavelet methods in computational fluid dynamics. *Annu. Rev. Fluid Mech.*, 42(1):473–503, 2010.

T. Schuller, D. Durox, and S. Candel. Dynamics of and noise radiated by a perturbed impinging premixed jet flame. *Combust. Flame*, 128:88–110, 2002.

I. W. Selesnick, R. G. Baraniuk, and N. G. Kingsbury. The dual-tree complex wavelet transform. *IEEE Signal Proc. Mag.*, 22:6:123–151, 2005.

I.G. Shepherd. Flame surface density and burning rate in premixed turbulent flames. *Proc. Combust. Inst.*, 26:373–379, 1996.

S. H. Sohrab, Z. Y. Lee, and C. K. Law. An experimental investigation on flame interaction and the existence of negative flame speeds. *Proc. Combust. Inst.*, 20: 1957–1965, 1984.

C. J. Sun and C. K. Law. On the consumption of fuel pockets via inwardly propagating flames. *Twenty-Seventh Symposium (International) on Combustion*, 27:963–970, 1998.

J. C. Sutherland and C. A. Kennedy. Improved boundary conditions for viscous, reacting flows. *J. Comput. Phys.*, 191:502–524, 2003.

M. Talei, M. J. Brear, and E. R. Hawkes. A parametric study of sound generation by premixed laminar flame annihilation. *Combust. Flame*, 159:757–769, 2012.

F. A. Williams. *Combustion theory: the fundamental theory of chemically reacting flow systems*. Number 1 in Combustion science and engineering series. Perseus Books, 1994.

C. S. Yoo and H. G. Im. Characteristic boundary conditions for simulations of compressible reacting flows with multi-dimensional, viscous reacting effects. *Combust. Theor. Model.*, 11:2:259 – 286, 2007.

Table 1: Thermo-chemical parameters.

s_L (ms^{-1})	δ_{th} (mm)	δ (mm)	τ_f (ms)	T_{in} (K)	τ
0.6034	0.430	0.121	0.713	600	2.52

Table 2: DNS parameters

Case	Type	u'_{in}/s_L	$\overline{u}_{in}/s_L$	Re_{l_0}	l_0/δ_{th}	Ka	Da
TV06	twin	6.0	16.6	94	3.1	4.4	0.51
TV10	twin	10.0	16.6	114	2.2	11.3	0.22
TVFS	twin	15.0	16.6	63	0.8	34.4	0.05

Table 3: Mean interaction length scales $\overline{L_{int}^{V+}} = \overline{\Phi^{1/3}}$ and $\overline{L_{int}^{S+}} = \overline{\phi^{1/2}}$ by type for all flames.

Case	L_{CN}^{V+}	L_{CX}^{V+}	L_{TC}^{V+}	L_{PB}^{V+}	L_{CN}^{S+}	L_{CX}^{S+}	L_{TC}^{S+}	L_{PB}^{S+}
TV06	0.75	1.30	1.16	1.12	2.20	3.89	3.27	2.68
TV10	0.74	1.25	1.26	0.98	2.07	3.77	3.66	2.28
TVFS	-	1.08	1.11	1.12	-	3.11	3.06	2.73

Table 4: Normalised mean and rms global stretch rates for all cases.

Case	$\overline{K}^{+}$	$\overline{K}_F^{+}$	$\overline{K}_{INT}^{+}$	$\overline{K}_{CN}^{+}$	$\overline{K}_{CX}^{+}$	$\overline{K}_{TC}^{+}$	$\overline{K}_{PB}^{+}$	K^{+rms}	K_F^{+rms}	K_{INT}^{+rms}
TV06	0.022	0.103	-0.080	-0.001	-0.015	-0.047	-0.017	0.572	0.532	0.148
TV10	0.038	0.170	-0.132	-0.003	-0.019	-0.087	-0.015	0.663	0.651	0.169
TVFS	-0.022	-0.001	-0.020	0.000	0.001	-0.015	-0.006	0.342	0.330	0.055

List of Figures

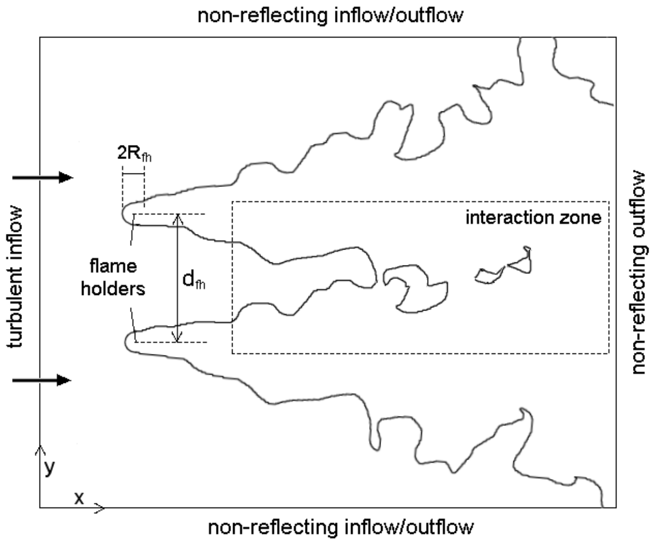

Figure 1: Schematic layout of computational domain.

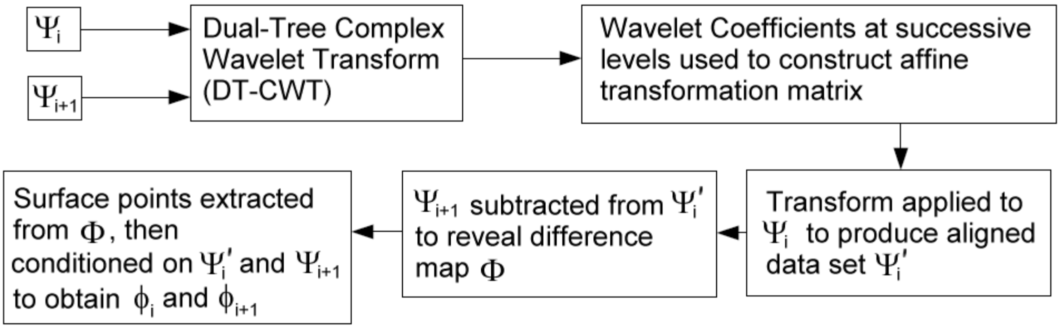

Figure 2: Flowchart summary of the automatic feature extraction procedure.

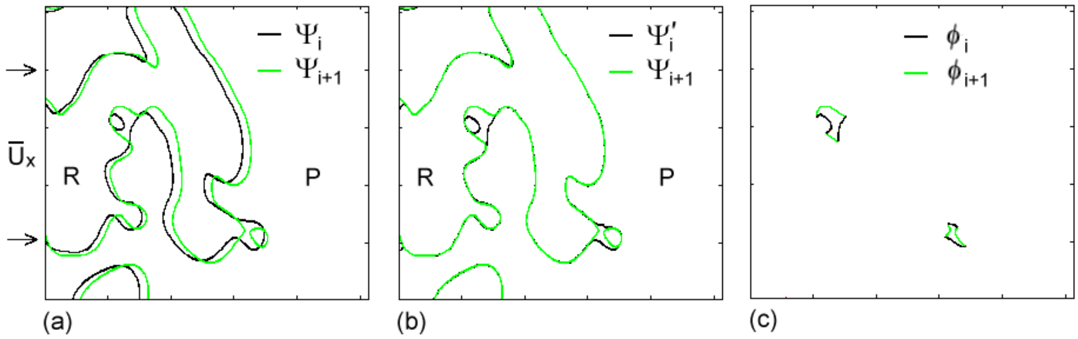

Figure 3: Automatic feature extraction applied to a 2-dimensional flame data at times t_i and t_{i+1}. The mean flow is from left to right. Reactants and products are denoted R and P respectively. (a) Original data Ψ_i and Ψ_{i+1} representing product regions. (b) Data at t_i is registered to data at t_{i+1} to produce Ψ_i'. (c) Two CX type interactions are extracted and surface points ϕ_i and ϕ_{i+1} identified (see section 4.1).

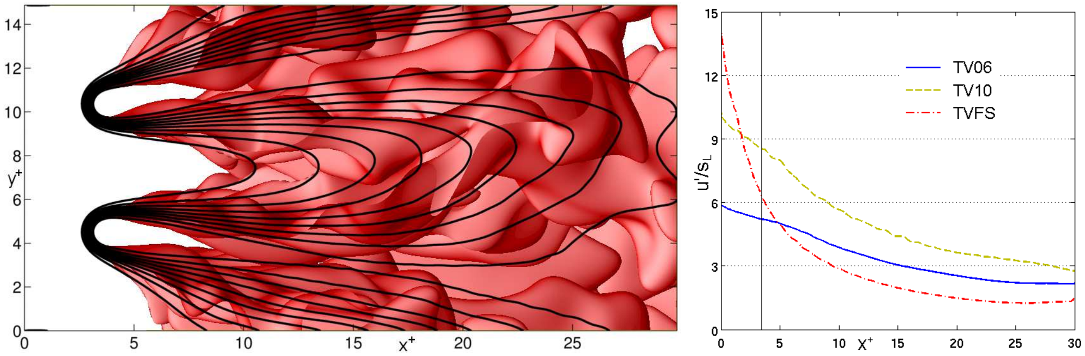

Figure 4: (a) Snapshot of the 3D $c = 0.8$ isosurface overlaid with contours of $\tilde{c}$ at $\tilde{c} = 0.1, 0.2, ..., 0.9$ for flame TV06; (b) Turbulence intensity u'/s_L along centre line of domains ($y^+ = 7.44$) for all flames. Vertical line indicates position of flame-holder.

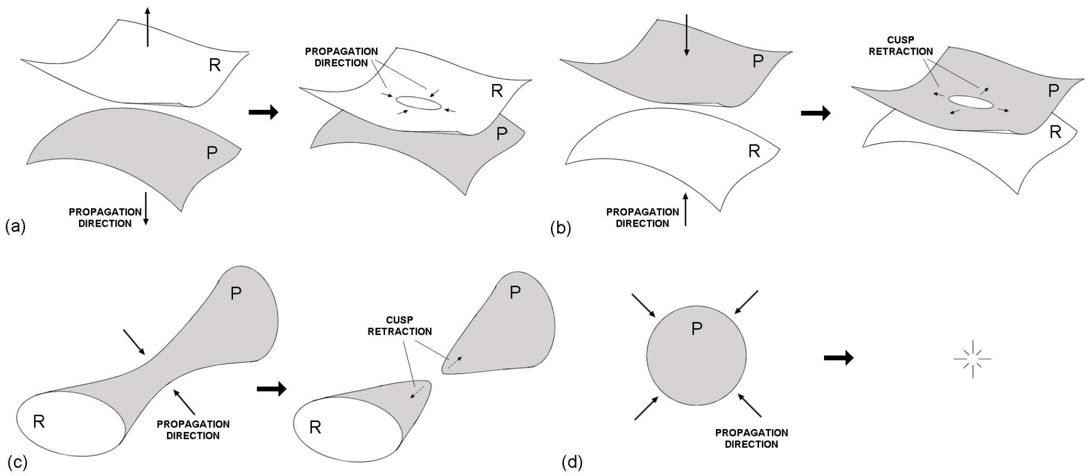

Figure 5: Schematic illustrations of (a) counter-normal (CN), (b) convex-normal (CX), (c) tunnel closure (TC), and (d) pocket burn-out (PB) type interactions. R and P denote reactants and products respectively.

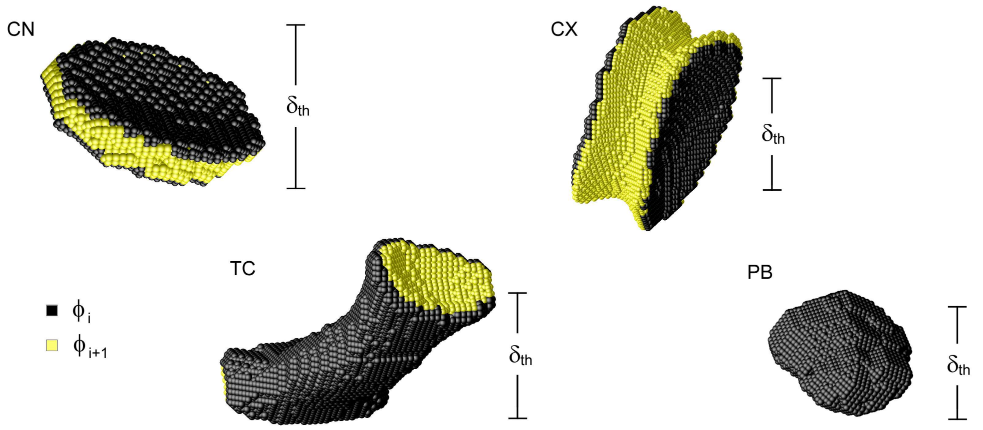

Figure 6: Examples of data extracted using AFE for each interaction type from the TV06 flame. Data points in ϕ_i and ϕ_{i+1} are represented by black and yellow spheres respectively. Scale indicated by laminar flame thickness δ_{th} for each image.

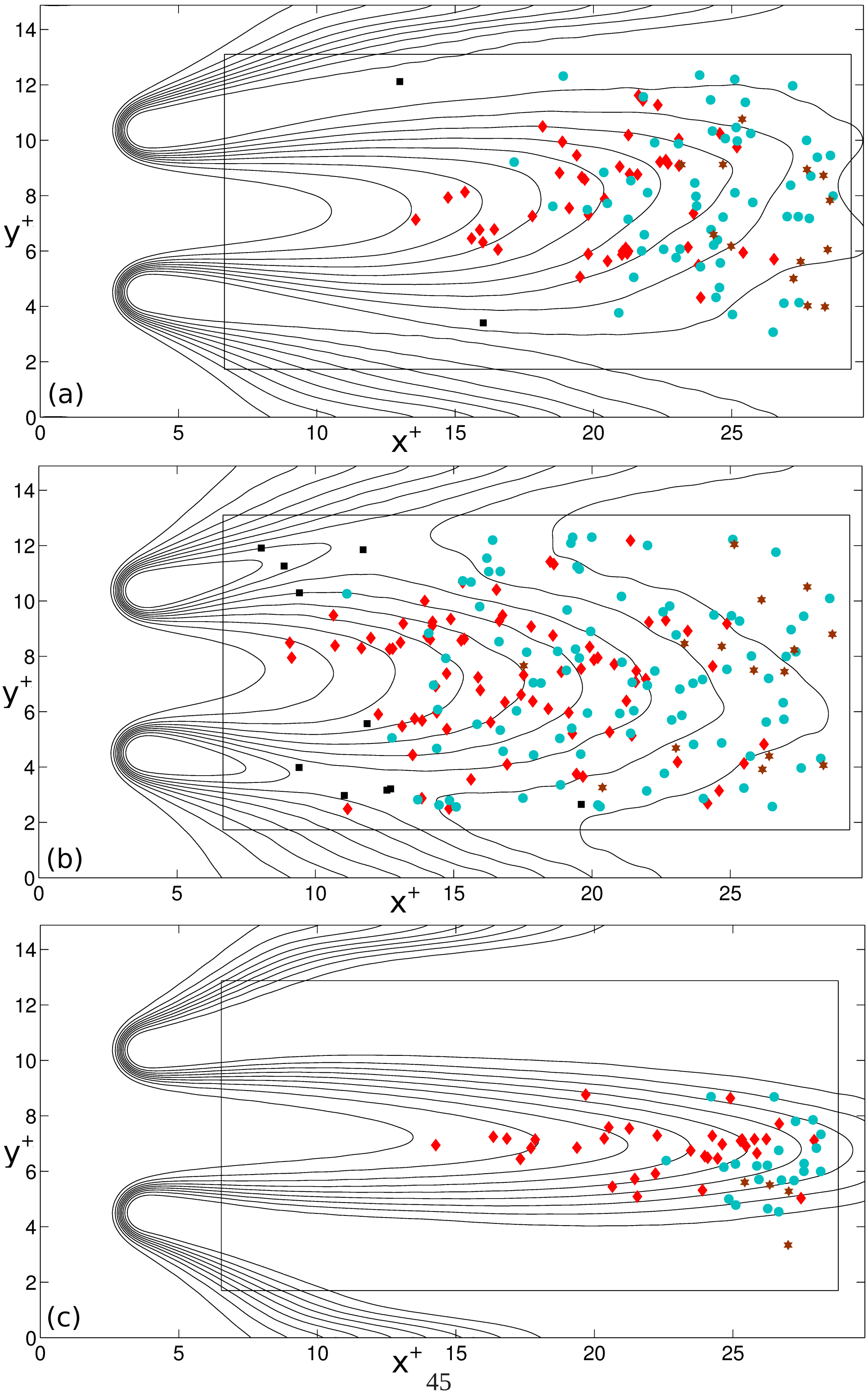

Figure 7: Contours of $\tilde{c}$, for $\tilde{c} = 0.1, 0.2, ..., 0.9$, for case TV06 (a), TV10 (b), and TVFS (c). Interaction types are CN (black squares), CX (red diamonds), TC (blue circles) and PB (brown stars). Rectangle shows region over which AFE was applied.

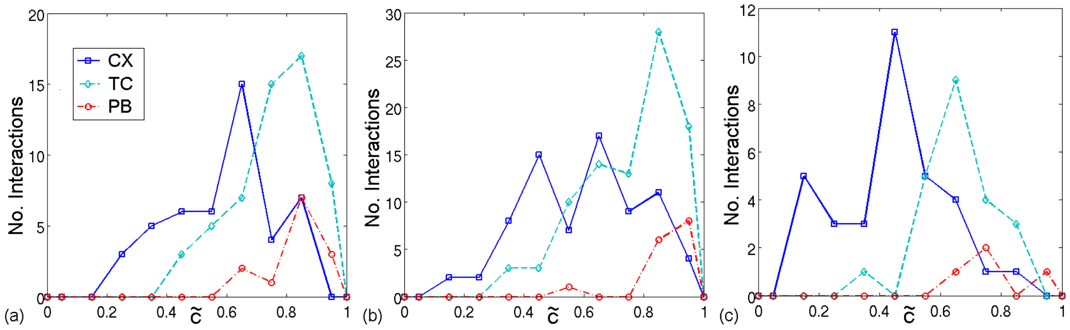

Figure 8: Number of interactions occurring by type in 10 evenly spaced bins of $\tilde{c}$ for flames TV06 (a), TV10 (b) and TVFS (c).

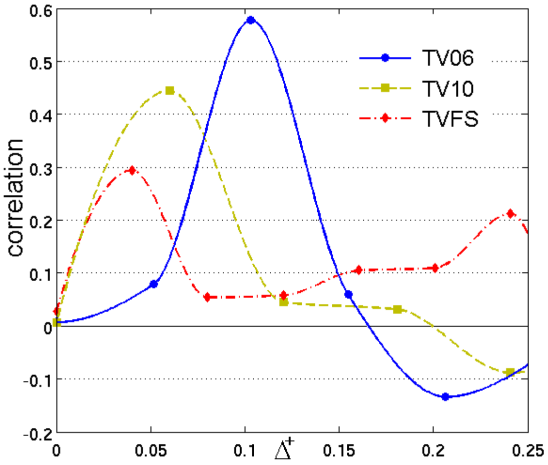

Figure 9: Interaction frequency correlations as a function of normalised delay time Δ^+ for CX-TC events. Correlations are evaluated at discrete points marked by symbols. Shape-preserving splines have been added for readability.

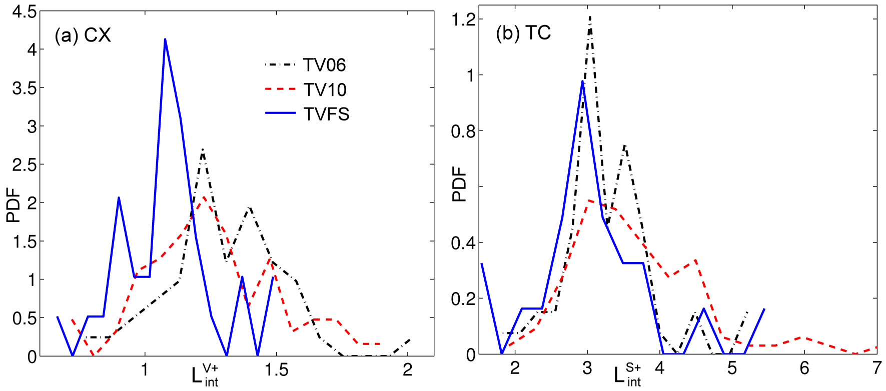

Figure 10: Probability densities of interaction length scales for all cases: a) L_{int}^{V+} for CX interactions, b) L_{int}^{S+} for TC interactions.

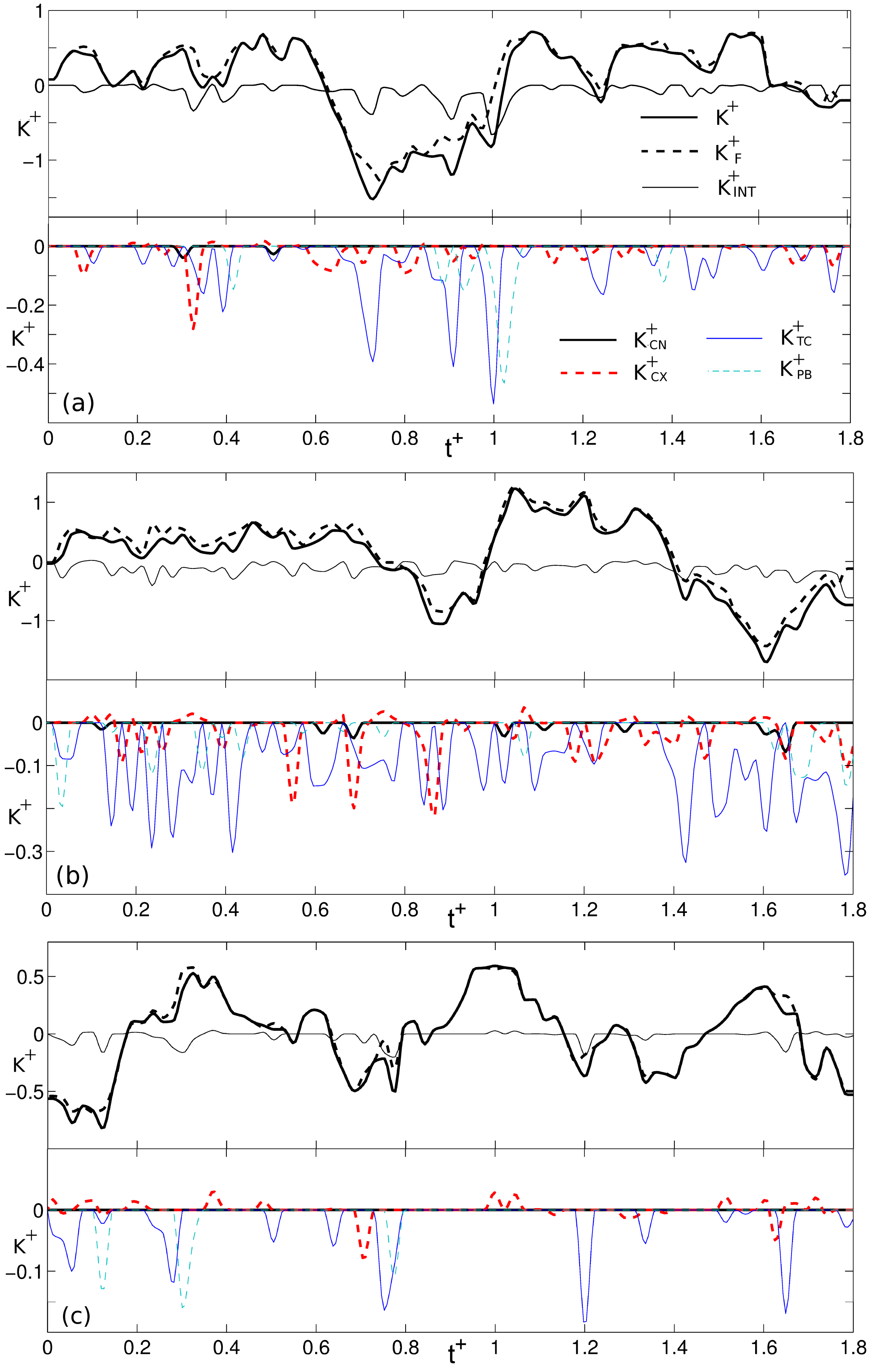

Figure 11: Normalised stretch rates, $K^+ = K\tau_f$, on the $c = 0.8$ isosurface for cases TV06 (a), TV10 (b), and TVFS (c). Top: total stretch rate, K^+, flamelet component, K_F^+ , and interactions component, K_{INT}^+. Bottom: interaction stretch rates by type.